



The primacy of temporal dynamics in driving spatial self-organization of soil iron redox patterns

Xiaoli Dong^a, Daniel D. Richter^b, Aaron Thompson^c, and Junna Wang^{a,1}

Edited by François Morel, Princeton University, Princeton, NJ; received August 22, 2023; accepted November 13, 2023

This study investigates mechanisms that generate regularly spaced iron-rich bands in upland soils. These striking features appear in soils worldwide, but beyond a generalized association with changing redox, their genesis is yet to be explained. Upland soils exhibit significant redox fluctuations driven by rainfall, groundwater changes, or irrigation. Pattern formation in such systems provides an opportunity to investigate the temporal aspects of spatial self-organization, which have been heretofore understudied. By comparing multiple alternative mechanisms, we found that regular iron banding in upland soils is explained by coupling two sets of scale-dependent feedbacks, the general principle of Turing morphogenesis. First, clay dispersion and coagulation in iron redox fluctuations amplify soil Fe(III) aggregation and crystal growth to a level that negatively affects root growth. Second, the activation of this negative root response to highly crystalline Fe(III) leads to the formation of rhythmic iron bands. In forming iron bands, environmental variability plays a critical role. It creates alternating anoxic and oxic conditions for required pattern-forming processes to occur in distinctly separated times and determines durations of anoxic and oxic episodes, thereby controlling relative rates of processes accompanying oxidation and reduction reactions. As Turing morphogenesis requires ratios of certain process rates to be within a specific range, environmental variability thus modifies the likelihood that pattern formation will occur. Projected changes of climatic regime could significantly alter many spatially self-organized systems, as well as the ecological functioning associated with the striking patterns they present. This temporal dimension of pattern formation merits close attention in the future.

environmental variability | iron dynamics | pattern formation | soil mottles | Turing instability

Redoximorphic features are observed in soils worldwide (1, 2). During anoxic periods, reduced iron [Fe(II)] moves in soil pore water and when oxidized to Fe(III), forms redoximorphic features often characterized by the distinct presence (orange) or absence (gray) of Fe(III) (3) (Fig. 1). While redoximorphic features mostly occur in soils that are frequently flooded, in drier upland soils, tiger-stripe-like patterns, alternating between horizontal Fe-depleted gray bands and Fe-oxide-rich orange bands, have been reported (4–7) (Fig. 1A and SI Appendix, Table S1). The mechanisms responsible for these patterns remain unknown. Regular patterns, however, are commonplace in many ecosystems, and several theories have emerged to explain them (8–11). Most notably, rhythmic banding also forms in dryland vegetation (8, 12, 13) and in rocks and weathering minerals (14, 15). The former has been explained by Turing instability (16) and the latter by the Liesegang mechanism (14). Here, we investigate the mechanisms forming regular iron bands, an as yet unexplained phenomenon in soils around the world (4–6), through the lens of Turing morphogenesis. This framework of pattern formation involves an inhibitor and an activator (16). The activator promotes local increases in both itself and the inhibitor, whereas the inhibitor acts to inhibit and reduce concentrations of the activator. Classic Turing patterns emerge with differential movement of the activator and inhibitor and have been investigated in many ecosystems (11, 17–21).

Environmental variability has rarely been considered previously in spatially self-organized systems. Temporal dynamics of the environment likely plays a pivotal role in iron band formation in upland soils. Upland soils undergo significant redox fluctuations driven by rainfall, groundwater table changes, or irrigation (22, 23) and redox conditions in turn dictate soil biogeochemistry. Environmental variability creates conditions for distinct processes, e.g., reduction and oxidation, to occur at the same site, over the timescales relevant to pattern formation, although separated in time. Environmental variability further determines the duration of the temporal windows, thereby controlling rates of various pattern-forming processes relative to each other averaged over a given period. Since formation of regular patterns often requires a specific ratio of process rates (12, 16), environmental variability can thus alter the likelihood of pattern formation. In the context of Turing morphogenesis (16), the activator increases the concentrations of itself and of the

Significance

Iron reactions create redox features in soils worldwide. We investigate mechanisms forming regularly spaced horizontal iron bands in upland soils. Upland soil redox conditions, driven by environmental variability, are highly dynamic. We found that redox fluctuations facilitate the formation of iron bands through two coupled scale-dependent feedbacks, consistent with Turing morphogenesis. Environmental variability creates distinct conditions for pattern-forming processes to occur at separate times and determines the duration of each process. Consequently, environmental variability dictates the ratio of the rates of various processes involved in pattern formation and the likelihood that iron banding will occur. Such a critical role of the temporal dimension in spatial self-organization has rarely been reported and holds potential explanatory power in other self-organized systems.

Preprint Servers: bioRxiv (https://www.biorxiv.org/ content/10.1101/2023.03.28.534585v2.full.pdf).

Author contributions: X.D., D.D.R., A.T., and J.W. designed research; X.D. and J.W. performed research; and X.D., D.D.R., A.T., and J.W. wrote the paper.

The authors declare no competing interest.

This article is a PNAS Direct Submission.

Copyright © 2023 the Author(s). Published by PNAS. This article is distributed under Creative Commons Attribution-NonCommercial-NoDerivatives License 4.0

¹To whom correspondence may be addressed. Email: jnawang@ucdavis.edu.

This article contains supporting information online at https://www.pnas.org/lookup/suppl/doi:10.1073/pnas. 2313487120/-/DCSupplemental.

Published December 14, 2023.

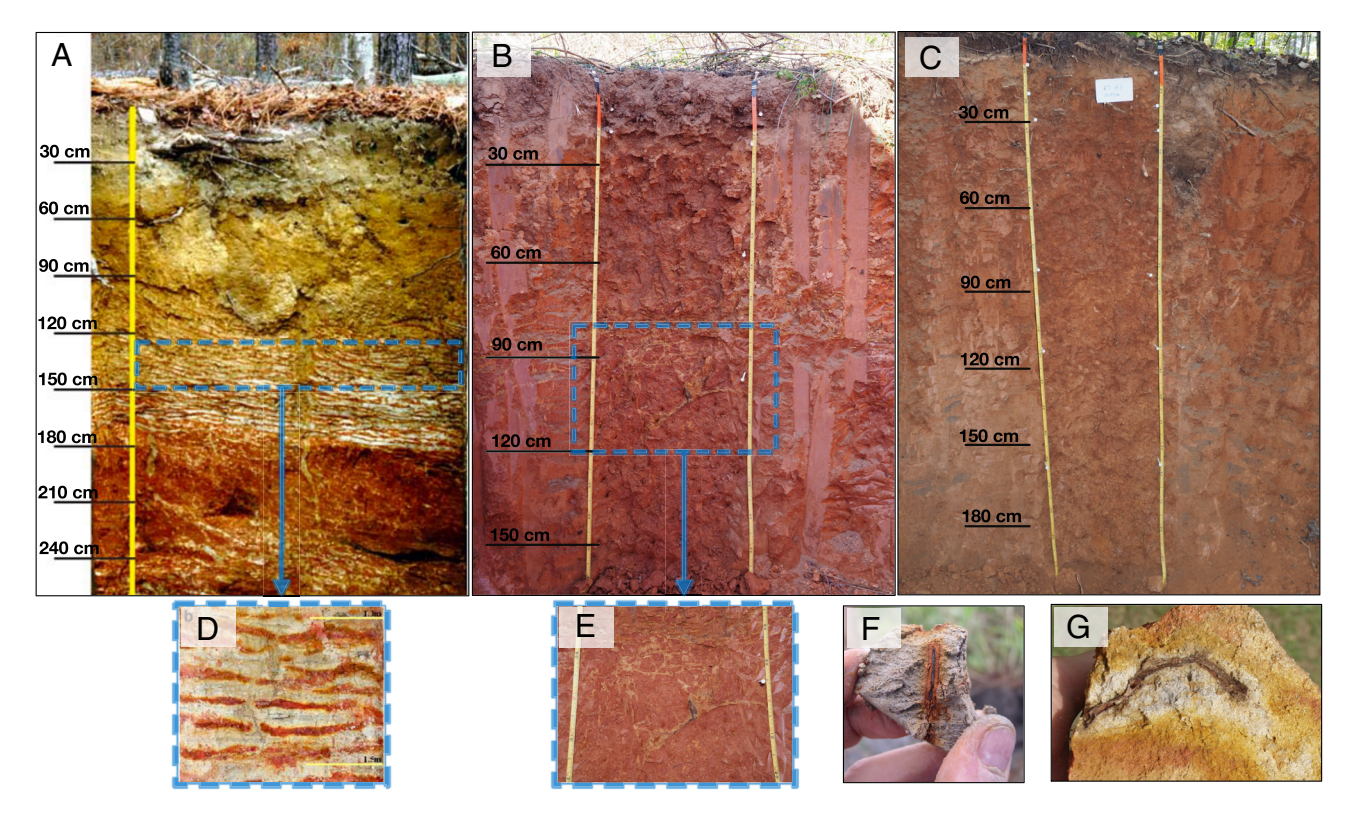


Fig. 1. Variations of iron redox patterns in soils. (*A*) Our study site with extensive regular patterns; (*B*) A site nearby (~4,000 m) our study site showing narrow, irregular redox patterns; (*C*) A site nearby (~400 m) our study site without any patterning. The close-up views of pattern zones in *A* and *B* are presented in *D* and *E*. (*F*) rhizosphere creates an oxidized orange zone in wetland soils, while (*G*) rhizosphere creates a reduced gray zone in upland soils. Patterns shown in *A–E* are all from the Calhoun Long-term Soil Experiment Forests in South Carolina.

inhibitor, both of which then diffuse along concentration gradients. Regular patterns can emerge only when the inhibitor diffuses faster than the activator. Such differences in diffusion rates represent the essence of Turing morphogenesis and scale-dependent feedbacks (SDFs)—the activator increases its own concentration locally (short-range positive feedback) while the inhibitor inhibits the expansion of the activator distally (long-range negative feedback). The temporal dimension of pattern formation is thus crucial but has been heretofore rarely investigated.

We examined the mechanism forming regular iron bands in soils. Our study site is at the Calhoun Experimental Forest, South Carolina. At this site, coarse-textured and porous A and E horizons overlie kandic Bt-horizons that are dominated by kaolinite and Fe and Al oxide minerals. The study area receives an annual rainfall of ~1,270 mm. Rainfall periodically exceeds evapotranspiration and leads to low oxygen concentrations, especially in the Bt horizons, where perched water tables emerge during the winter and early spring. With sufficient organic reductants present, microbial decomposition can locally consume the dissolved oxygen and prompt a switch to respiration via Fe(III) reduction with subsequent release and mobilization of highly soluble Fe(II) in the aqueous phase (4, 7). A pattern of alternating gray and orange horizontal bands, with bandwidth of ~1.6 cm (Fig. 1 A and D), is located between the soil depths of 1.0 and 1.8 m (in the Bt horizons). The gray bands are low in Fe(III) but are rich in clay-sized minerals (kaolinite) and soil organic carbon (SOC) (SI Appendix, Table S2) and harbor abundant fine roots and hyphal networks of mycorrhizal fungi. In contrast, the orange bands are high in Fe(III) and low in clay-size particles and SOC, with no signs of root growth or ectomycorrhizal hyphae. The crystallinity of Fe(III) minerals in the orange bands is much higher than that in the gray bands. A thorough description of geochemical properties of the redox bands at

our study site is provided elsewhere (4, 7). Here, using generalized Turing morphogenesis models, we show that iron bands in upland soils are generated by coupling two sets of SDFs and that redox fluctuations play an indispensable role in their formation.

Results

Mechanisms of Pattern Formation. We constructed models consisting of two modules. The first module captures soil water dynamics ("Soil Water Dynamics" in Methods), which are driven by historical rainfall and evapotranspiration records and simulates soil moisture fluctuations, potential redox oscillations, and hydrodynamic flow. The second module describes soil biogeochemical changes, involving root growth (source of organic matter, OM), chemical reactions among Fe(II), Fe(III), O2, and OM and their transport, and changes of clay content. Repeated redox fluctuations induce evolution of phases of Fe(III) crystallinity and clay dispersion/ coagulation during iron redox oscillations (24–27). These processes constitute core pattern-forming feedback that we describe in more detail below. While also belonging to reactive transport models (28-30), models in this study focus on Turing morphogenesis they incorporate scale-dependent feedbacks (SDFs) consisting of an inhibitor, an activator, and their relative transport rates. We compared three categories of mechanisms (Fig. 2): a) SDFs with the long-range negative feedback realized by threshold-dependent root responses to highly crystalline Fe(III), coupled with another SDFs mediated by clay dispersion/coagulation (Movie S1). We also examined whether each set of SDFs alone is sufficient to form iron bands (Movies S2 and S3); b) SDFs with the negative feedback realized by monotonic root growth responses to soil moisture (Movie S4); and c) a template effect of root structure, i.e., iron banding formed following the pre-existing root spatial structure, without invoking any SDFs (Movie S5).

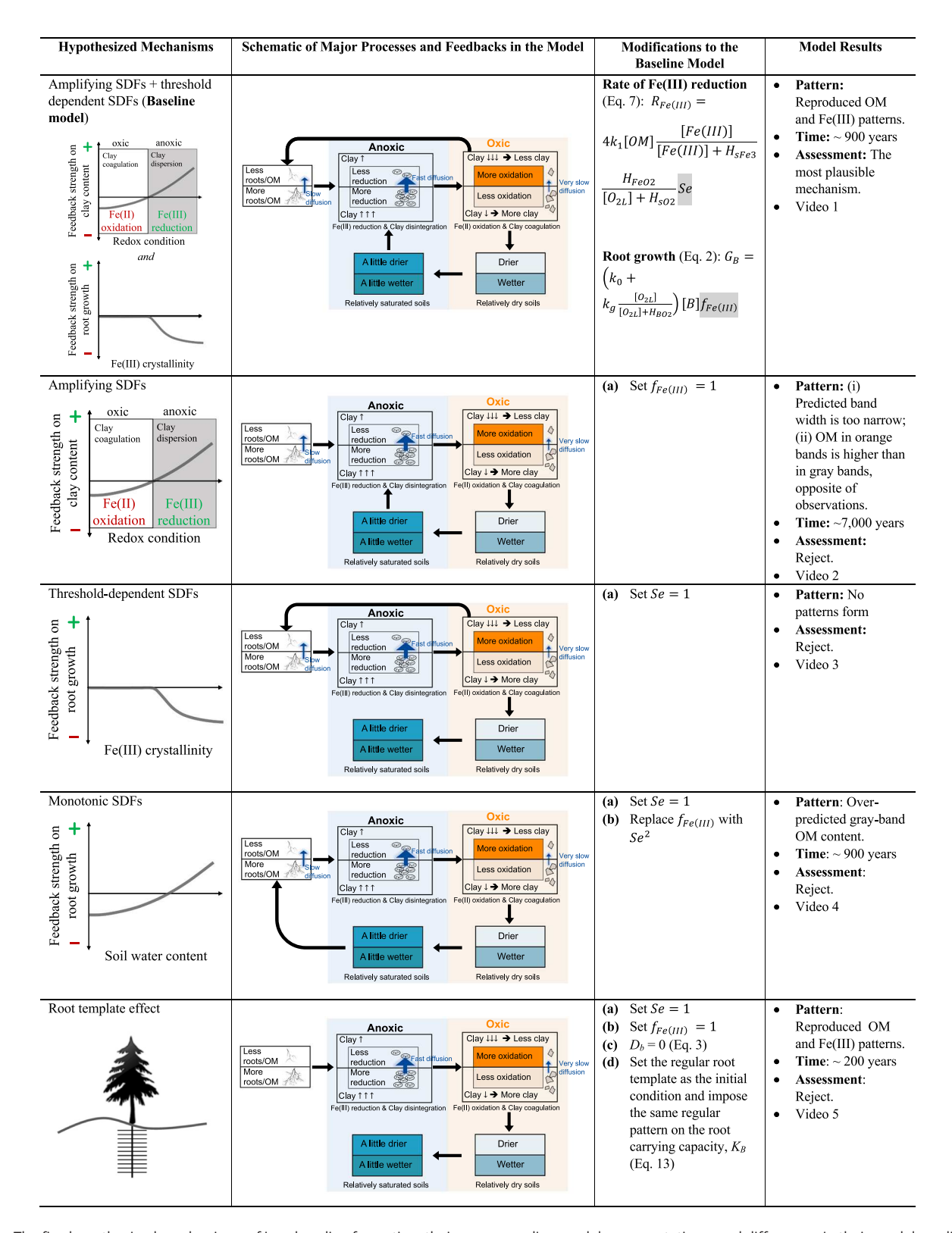


Fig. 2. The five hypothesized mechanisms of iron banding formation, their corresponding model representations, and differences in their model predictions. In the second column, two stacked boxed represent two layers (microsites) of soils in the vertical direction, starting with the upper layer containing slightly less organic matter (OM) and the lower layer containing slightly more OM. In the third column, the terms that are modified in the baseline model are highlighted in gray.

Threshold-dependent SDFs form regular bands. Fluctuations in soil moisture induce changes in soil redox, thereby generating a repeating alternation of oxidizing and reducing conditions. Such redox oscillations that bias periods of oxidation can promote precipitation of Fe(III) of increasing crystallinity (24). Over repeated redox oscillations of this type, Fe(III) can cement into plinthite-like material (31–33) that is common in soils in the study region. While

roots possess an array of morphological and chemical adaptations to penetrate soils (34, 35), hard and brittle plinthite-like material forms a barrier to root penetration (36, 37). At our study site (4) and other sites (5) with similar iron bands, the crystallinity of goethite in orange bands is significantly higher than in gray bands (38), with the ratio of ammonium-oxalate extractable Fe and dithionite-extractable Fe falling in the range for plinthite and ironstone concretions. Previous work (4) shows that i) fine roots grow exclusively in the gray bands and ii) SOC in the gray bands is much younger than SOC in the orange bands (based on radiocarbon dating), further supporting the absence of recent root growth in the orange bands. Based on these observations, we use a threshold-dependent scaler, $f_{Fe(III)}$ (between 0 and 1; unitless; Fig. 2), to describe the effect of Fe(III) on root growth, G_B (g m⁻³ d⁻¹):

in *Methods*). Rate of Fe(II) oxidation, $R_{Fe(II)}$ (mol m⁻³ d⁻¹), is modeled using kinetic laws as a function of Fe(II) and O_{2L} (Eq. **10** in *Methods*). Fe(III) reductive dissolution, $R_{Fe(III)}$ (mol m⁻³ d⁻¹), is complex and affected by many factors such as competitive and synergistic effects of ion adsorption on the mineral surface (44). Such surface processes are particularly important for kinetics of rock weathering, as significant evolution of exposed mineral

$$f_{Fe(III)} = \begin{cases} 1, & [Fe(III)] \leq [Fe(III)]_{ng} \\ \frac{H_{BFe}^2}{H_{BFe}^2 + \left([Fe(III)] - [Fe(III)]_{ng} \right)^2}, & [Fe(III)] > [Fe(III)]_{ng} \end{cases},$$
[1]

$$G_B = \left(k_0 + k_g \frac{[O_{2L}]}{[O_{2L}] + H_{BO2}}\right) [B] f_{Fe(III)},$$
 [2]

where $[Fe(III)]_{ng}$ denotes the threshold Fe(III) content (mol m⁻³), above which root growth is negatively affected. While aggregation of [Fe(III)] does not increase its crystallinity per se, in repeated precipitation/dissolution sequences, increases in Fe(III) aggregation and in crystallinity often coincide (24, 39), especially in sequences favoring slow oxidation in the presence of crystalline iron phases (38), such as exist in our study site (39). H_{BFe} (mol m⁻³) is the half-saturation constant regulating the effect of Fe(III) on root growth. Here, we assume that root growth, G_B , is affected by dissolved oxygen $[O_{2L}]$ (mol m⁻³) and mechanical impedance by highly crystalline Fe(III) aggregates (40, 41) (Eq. 2). The term [B] (g m⁻³) is root biomass density, k_0 (d⁻¹) is the root growth rate constant, and k_g (d⁻¹) is that part of growth affected by $[O_{2L}]$. Reactive transport of $[O_{2L}]$ is modeled in Eq. 16 (*Methods*).

In addition to growth (G_B) , changes of [B] are affected by 1) respiration, R_B , 2) OM deposition from root residues, M_B (R_B is affected by $[O_{2L}]$ and [B]; M_B is proportional to [B]; see Eqs. 12 and 13 in *Methods*), and 3) biomass expansion to neighboring locations, often approximated by a diffusion process (42, 43):

$$\frac{\partial [B]}{\partial t} = G_B - R_B - M_B + D_b \frac{\partial^2 [B]}{\partial z^2},$$
 [3]

where D_b is the biomass diffusion coefficient (m² d⁻¹). Importantly, the accrual of B also produces OM (changes of OM are modeled by its accumulation via M_B and its loss to O_2 and Fe(III) oxidation; see Eqs. **14** and **15** in *Methods*). OM can reduce Fe(III) in the soil, when O_2 is depleted:

$$Fe(OH)_{3(s)} + \frac{1}{4}CH_2O + 2H^+ \rightarrow Fe^{2+} + \frac{1}{4}CO_2 + 2\frac{3}{4}H_2O,$$
[4]

Fe(II) diffuses from the rhizosphere and along the way can be readily oxidized in the presence of O_2 :

$$\text{Fe}^{2+} + \frac{1}{4}\text{O}_2 + 2\frac{1}{2}\text{H}_2\text{O} \rightarrow \text{Fe}(\text{OH})_{3(s)} + 2\text{H}^+,$$
 [5]

$$\frac{\partial [Fe(II)]}{\partial t} = R_{Fe(III)} - R_{Fe(II)} + \frac{\partial (q_L[Fe(II)])}{\partial z} + D_{Fe(II)} \frac{\partial^2 [Fe(II)]}{\partial z^2},$$
 [6]

where $D_{Fe(II)}$ is the diffusion coefficient (m² d⁻¹) of Fe(II). The term q_L is the advection of soil water (m d⁻¹), supported by solving the Richards equation in the soil water dynamics module (Eqs. 19–23

surface area occurs over the course of weathering. We instead focus on processes driven by repeated redox oscillations in biologically active soils and assume that the Fe(III) reduction rate is affected by the availability of O_{2L}, OM, and Fe(III) (45–47). Fe (III) reduction is negligible until O_{2L} becomes scarce (~0.02 mol m⁻³) (48). Rate of reduction is further enhanced by soil water content (*SI Appendix*, Fig. S1) (49), as moisture can stimulate the activity of Fe(III)-reducing microorganisms (50) and increase the ratio of rapidly reducible Fe(III) to total Fe(III) in the soil (51, 52). At our study site, microsites of higher moisture are associated with lower Fe(III) crystallinity (*SI Appendix*, Fig. S2) (4). Fe(III) reduction rate often scales with the crystallinity of the iron phases, with the less-crystalline Fe(III) phase being more available for microbial reduction (45, 50, 53). Based on these lines of evidence, we modeled the rate of Fe(III) reduction by means of kinetic laws as follows:

$$R_{Fe(III)} = 4k_1[OM] \frac{[Fe(III)]}{[Fe(III)] + H_{sFe3}} \frac{H_{sO2}}{[O_{2L}] + H_{sO2}} Se, \quad [7]$$

where Se is normalized volumetric water content (see "Soil Water Dynamics" in Methods). k_I is the constant of the OM reductive rate (d⁻¹). H_{sFe3} and H_{sO2} are the half saturation constants (mol m⁻³) regulating the effect of Fe(III) and O_{2L} on the reduction rate, respectively.

In this model, roots act as the activator (Fig. 3A)—they simultaneously increase the concentration of themselves (Eq. 2) and of Fe(II), by supplying OM for reducing Fe(III). Fe(II) is the precursor of the inhibitor for root expansion: Fe(II) becomes the inhibitor when oxidized and when Fe(III) reaches the threshold of aggregation and crystallinity described in Eq. 1 and starts to inhibit root growth. According to Turing instability, if the rate of root expansion is slower than the diffusion of Fe(II) ($D_b < D_{Fe(II)}$), regular patterns can form. However, we found that the model did not produce any such pattern (*SI Appendix*, Fig. S3A). This is because the aggregation and crystallinity of Fe(III) phases must reach a high level before they can inhibit root growth. The ambient Fe(III) level of our system and most upland soils is far below that level. Thus, processes that can amplify the spatial heterogeneity of Fe(III) deposition are required before the banded patterns may form.

Amplifying heterogeneity. Redox oscillations not only alter Fe(III) crystallinity, but they also induce clay dispersion/coagulation (24–27). Microsites of higher clay content can retain more moisture than those with lower clay content (*SI Appendix*, Fig. S4) and hence are more likely to restrict O₂ diffusion and become anoxic and conducive for Fe(III) reduction. Fe(III) reduction leads to a transient increase in pH (Eq. 4), which can enhance the dispersion of silt-sized kaolinite clay particles (25), further increasing clay content. Consequently, in these microsites, clay content continues to increase while Fe(III) continues to decline by Fe(III) reduction. As Fe(II) diffuses along the concentration gradient, it is more

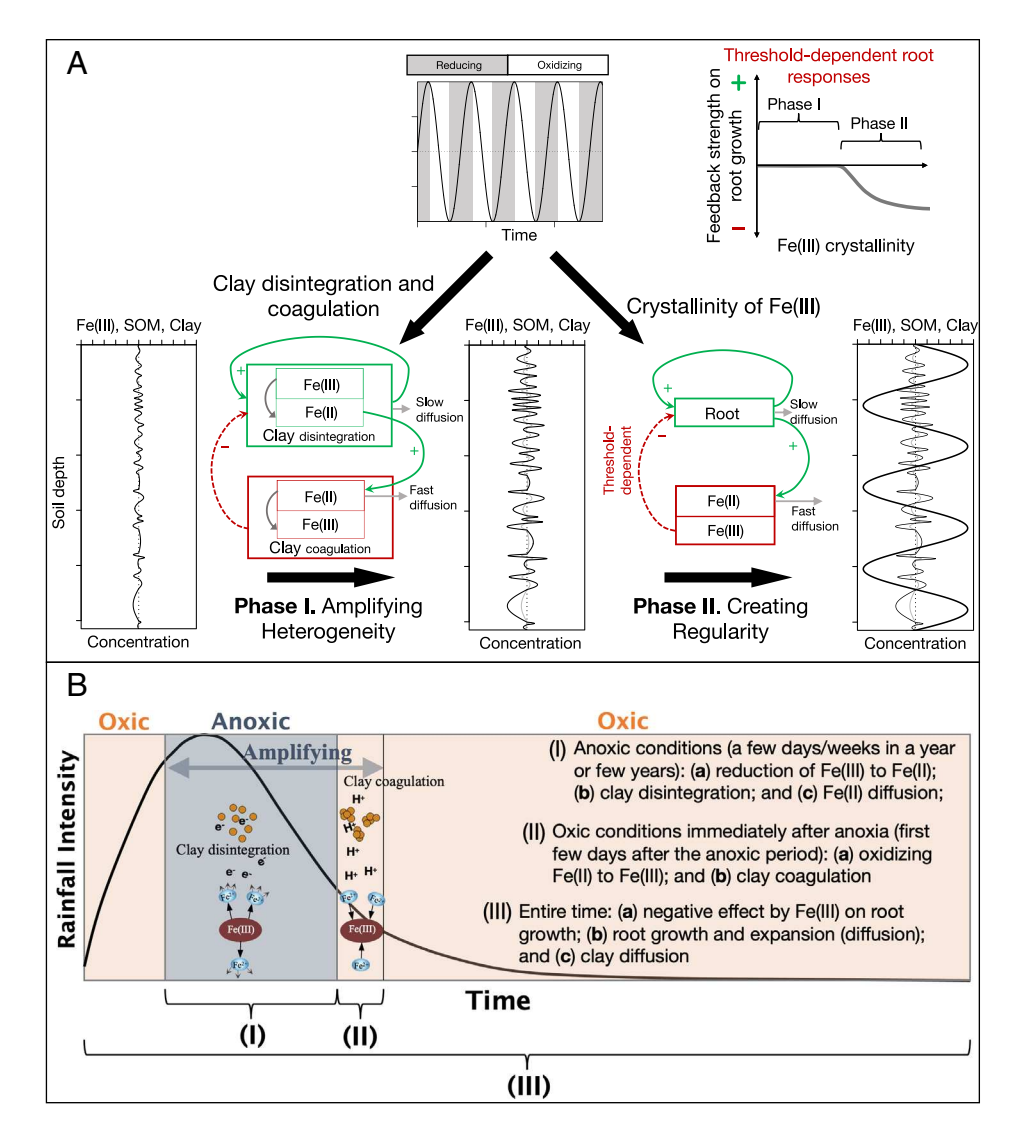


Fig. 3. (A) Schematic of the two-phase mechanism underlying redox pattern formation in upland soils—the initial amplifying scale-dependent feedback (SDF) phase and later threshold-dependent SDF phase. Soil redox oscillations play an indispensable role in both phases. (B) Distinct timescales of key pattern-forming

likely to be oxidized in microsites with lower clay contents because these microsites retain less moisture and will likely have higher O2 partial pressures. Fe(II) oxidation produces H⁺, lowers the pH, and triggers changes in the surface charge of the kaolinite clays that promote coagulation, reducing clay content (26). Consequently, in these microsites, clay content continues to decline while Fe(III) continues to accumulate, aggregate, and increase in crystallinity. These effects of clay content on soil water retention and moisture are supported by our field data (SI Appendix, Fig. S2) and are described in our model by having θ_s (saturated soil water content) and θ_r (residual water content) in the soil water dynamics module as functions of the evolving clay content (Eqs. 19–23 in Methods). The effect of soil moisture on Fe(III) reduction rate is captured by the term Se in Eq. 7. Wide shifts in kaolinite clay content by dispersion and coagulation accompanying iron reduction and oxidation have been well understood and established (25, 26, 54-56). Specifically, at our study site, soils with 1 mol m⁻³ lower Fe(III) correlate with a 0.0566% higher clay content (SI Appendix, Fig. S5). We used this empirical relationship to describe clay changes in a redox dynamic system:

$$\frac{\partial [CC]}{\partial t} = -0.0566 \frac{\partial [Fe(III)]}{\partial t} + D_c \frac{\partial^2 [CC]}{\partial z^2}, \quad [8]$$

$$\frac{d[Fe(III)]}{dt} = -R_{Fe(III)} + R_{Fe(II)}, \qquad [9]$$

where D_c is the clay diffusion coefficient (m² s⁻¹). It is important to note that clay dynamics are complex, affected by many variables, such as colloid type and size, surface properties, soil pore size, OM loadings, solution pH, and ionic strength (54, 57). Hence, the value of the constant in Eq. 8 likely varies with the system. However, the essence of the amplifying mechanism is the negative correlation between changes in clay and Fe(III) content. When this relationship is negative, as has been well established in the literature (25, 54-56) and observed at our site (4), the specific value of the constant, within a reasonable range, will unlikely change our result on the mechanism of pattern formation. Eq. 8, phenomenologically, but effectively captures clay dynamics during iron redox cycles in redox dynamic systems.

With clay dispersion/coagulation during iron redox oscillations amplifying Fe(III) heterogeneity, Fe(III) aggregation eventually reaches the threshold that negatively affects root growth. The model that couples the clay-mediated augmentation with thresholddependent SDFs reproduces all aspects of iron banding in the field, including a) spatial patterns, including the spatial extent of the pattern zone, width of orange and gray bands, and their spatial regularity (Fig. 4); b) profiles of Fe(III) and OM and the $\rm O_2$ profile during dry and wet periods (Fig. 4); c) time-series of $\rm O_2$ and soil water content (*SI Appendix*, Fig. S6); and (d) concentration contrasts of Fe(III), OM, biomass, clay, and soil water content between gray and orange bands (Fig. 4). The model slightly overpredicted Fe(III) and underpredicted OM in orange bands (*SI Appendix*, Table S2), likely because with the increase of Fe(III) in orange bands, the diffusion coefficient of Fe(II) might reduce, but this effect was not incorporated in our model due to lack of data. The model predicts that it takes ~900 y for patterns to form.

Amplifying SDFs alone form regular bands. Clay-mediated Fe(III) augmentation itself forms SDFs, with clay as the activator and Fe(II) the inhibitor (Fig. 3A). Pattern formation requires clay migration (diffusion in Eq. 8) to be slower than Fe(II) diffusion. However, using the model variant with the amplifying SDFs only (removing $f_{Fe(III)}$ in Eq. 2 to turn off the threshold-dependent SDFs), we found that formation of iron bands requires D_c to be at least six orders of magnitude lower than $D_{Fe(II)}$ (SI Appendix, Table S3). Such a dramatic difference in diffusion rate should be expected since Fe(II) exists primarily as a dissolved aqueous ion, and the clay particles are upward of 50 nm. The requirement of such a large difference in the mobility of clay and Fe(II) by this model variant is caused by the large difference in the durations of processes to augment Fe(III) heterogeneity and of those to smooth out the heterogeneity. Clay coagulation and dispersion augment Fe(III) heterogeneity during rapid pH changes in iron redox oscillations. However, Fe(III) reduction is limited to conditions of soil anoxia and Fe(II) oxidation is rapid during subsequent soil drying when O₂ is high (58). Consequently, processes that increase the heterogeneity of clay and Fe(III) operate for only a brief period in a year or even in several years, while diffusion of clay colloids, which

smooths out the heterogeneity, operates continuously (Fig. 3B). This model variant predicts pattern formation time of ~ 7,000 y, an order of magnitude longer than the time estimated by other mechanisms (Fig. 2). The very small D_c produced bandwidth ~1/3 of the width observed in the field. While the model can produce bandwidths comparable to those observed by increasing D_c , at larger D_c , for patterns to still form, a climate much wetter than our study area is required (longer duration of processes to create heterogeneity). This model predicts a higher OM in orange bands than in gray bands, opposite of the field observation (SI Appendix, Fig. S3C). Combined, our modeling suggests the observed iron bands are unlikely to be formed by this mechanism.

Monotonic SDFs form regular bands. We further tested the SDFs realized by a monotonic root growth and soil water relationship model, i.e., higher moisture stimulates root growth while lower moisture limits growth (Fig. 2). For this model variant, we removed Se in Eq. 7 to turn off the amplifying SDFs and replaced $f_{Fe(III)}$ with Se^2 in the root growth function (Eq. 2)—i.e., instead of threshold-dependent growth response to crystalline Fe(III), we assume monotonic root responses to soil moisture. In this model variant, roots acts as the activator—they increase themselves and produce the inhibitor Fe(II) by reducing Fe(III) with OM. Fe(II) oxidation induces clay coagulation, reducing clay content and soil water retention, and inhibiting root growth (captured by the new Se^2 in Eq. 2; Fig. 2). This model variant reproduces Fe(III) and clay patterns; however, it predicts enriched SOM in the gray bands compared to the ambient level (SI Appendix, Fig. S3D). Such an enrichment is not observed in the field.

Root template effect forms regular bands. Last, we tested whether the iron bands are a mere manifestation of the pre-existing root spatial structure (Fig. 2). For this model variant, we removed $f_{Fe(III)}$

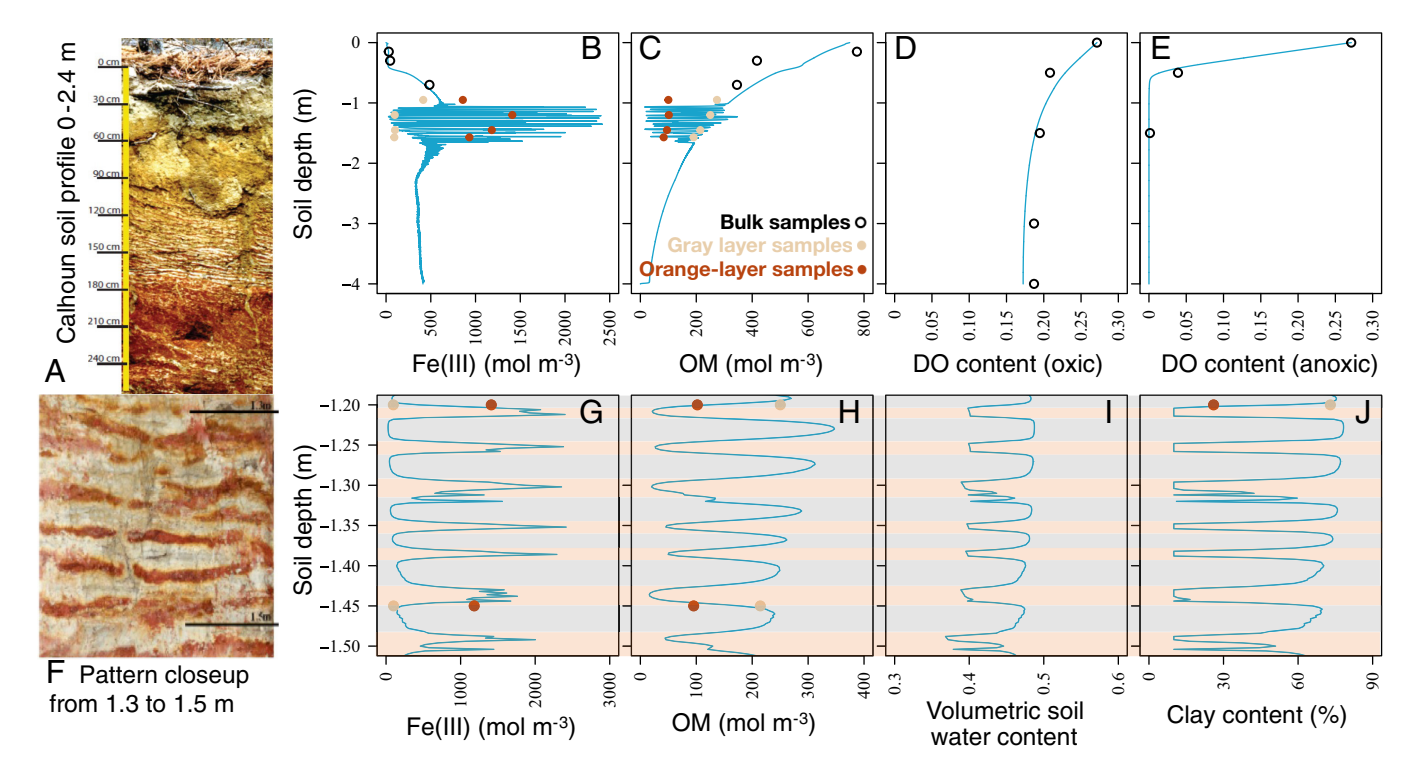


Fig. 4. Comparison between modeled and observed soil redox patterns. (*A*) Photo shows the regular iron banding at the study site at the Calhoun Experimental Forest. (*B*–*E*) blue lines denote modeled Fe(III) concentration (*B*), OM content (*C*), dissolved oxygen (DO) content under the oxic condition (*D*) and under the anoxic condition (*F*). Points in each plot denote field measurements from the study site, with dark brown denoting data from orange bands, and light yellow denoting data from gray bands. Open black circles represent bulk samples. (*F*) is the close-up view of the redox pattern between 1.3- and 1.5-m soil depth (*A*). (*G*–*J*) are close-up view between 1.2 and 1.5 m soil depth of the modeled Fe(III) concentration (*G*), OM content (*H*), soil water content (*I*), and clay content. (*J*). (*G*–*J*): layers of high Fe(III) show low OM, low soil water, and low clay content, while layers of low Fe(III) show high OM, high soil water, and high clay content. The DO profile in the oxic condition (*D*) and volumetric water content (*I*) are model results after 30 d of exposure to aerobic conditions.

in Eq. 2 and Se in Eq. 7 and set regularly spaced root distribution as the model initial condition. The steady-state pattern can mimic the regular root distribution in the initial condition (SI Appendix, Figs. S3E and S7), only under the condition of zero root biomass expansion (i.e., $D_b = 0$ in Eq. 3).

Conditions for Pattern Formation. With our preferred model (redox amplifying heterogeneity + threshold-dependent SDFs), we found that the iron bands are more likely to occur during relatively dry conditions and in soils with an intermediate clay content, i.e., rainfall < 3,500 mm y⁻¹ and clay content between 40% and 80% (Fig. 5). Climatic and soil conditions of sites from different parts of the world with similar iron bands fall within this domain (Fig. 5). Our modeling predicts that wet conditions and high clay content both accelerate Fe leaching and sandy soils will be overly well oxygenated, all reducing the likelihood of patterning. Model results further indicate that low clay content can be compensated for by high rainfall (Fig. 5).

Under the climatic condition of our site, our preferred model estimates that ~900 y is required to form regular iron bands. Given that the rainfall regime forcing the model is at the ~4-y recurrence interval, the actual pattern formation takes ~3,600 y. A longer pattern formation time is required in drier regions where the likelihood of wet conditions that can induce soil anoxia is lower. We found that pattern formation time increases exponentially with the decline of annual rainfall (SI Appendix, Fig. S8).

Consequences of Pattern Formation for Soil Carbon. Iron banding formation affects both the storage and fluxes of SOC. We found that formation of iron bands reduced SOC storage between 1.0 and 1.8 m of soil depths (pattern formation zone) by 24%. Results of our preferred model show that Fe(III) serves as an important electron accepter between December and May, when the evaporative demand is low (Fig. 6A). The model predicts that in a wet year (annual rainfall at the 70% percentile in 1951 to 2021), 10 to 50% of SOC could be oxidized by Fe(III) and the remainder by O₂ (Fig. 6B). Pattern formation creates the spatial segregation of SOC in gray bands and Fe(III) in orange bands. As a result, roughly, a potential capacity of ~1.72 t C ha⁻¹ y⁻¹ decomposition by Fe(III) is lost (0.43 t C ha⁻¹ y⁻¹ is estimated to be decomposed by Fe reduction for 20 cm soil depth according

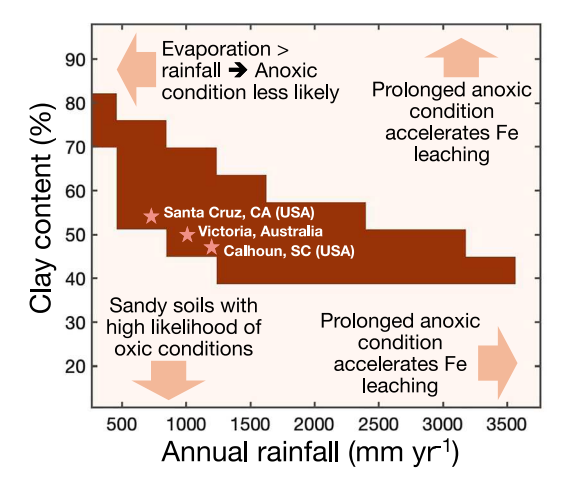


Fig. 5. Model-predicted domain of soil texture and annual rainfall to have regular iron redox bands in upland soils. The dark-brown polygon in the center delineates the domain predicted by the model where regular iron bands can emerge, with the locations of stars indicating the corresponding annual rainfall and clay content at the three sites where regular iron redox bands have been reported (SI Appendix, Table S1).

to ref. 58), comparable to the net primary productivity, 2 to 4 t C ha⁻¹ y⁻¹, for our system (58).

Discussion

Mechanism Forming Redox Bands. The most plausible mechanism forming regular iron bands in upland soils is the coupling of two sets of SDFs—clay coagulation and dispersion during iron redox oscillations augment Fe(III) aggregation and crystallinity (amplifying SDFs) to the level that suppresses root growth, triggering the threshold-dependent SDFs (Fig. 2). Plants possess an array of approaches to improve their root penetration in soils and small-particle, low-crystallinity Fe(III) in soil does not restrict root growth (34, 35). However, when Fe(III) develops into plinthite-like aggregates, they do become a barrier for root growth. Such threshold-dependent responses are common in nature (59-61), suggesting that coupled SDFs shown in this study might be generalizable to many spatially self-organized systems.

The amplifying SDF model mediated by clay coagulation and dispersion alone can also form iron bands; however, predicted bandwidth and patterns of OM and Fe(III) do not match field observations (SI Appendix, Fig. S3C). Similarly, while the SDF model realized by monotonic root responses to soil moisture can also form iron bands, this model overpredicts gray-band OM (SI Appendix, Fig. S3D), because of the hypothesized positive root responses to high moisture. If we assume no such positive responses, but only an inhibitory effect by moisture below a certain level, i.e., a threshold-dependent, instead of monotonic, response, the model would no longer overpredict OM. However, in that case, no pattern forms because volumetric soil water content in our study area is high, ranging between ~38% and 43% at 0.5-m depth year around (*SI Appendix*, Fig. S6). At such a high moisture level, root growth is unlikely inhibited by water availability (62), resulting in the lack of the inhibitor in Turing instability. This mechanism however can likely form iron bands in drier soils, where growth is water limited, as it has for regular vegetation patterns in drylands (12, 43).

The root template hypothesis is unlikely (Fig. 2). For iron bands to be a mere reflection of preexisting root structure, it requires i) a regularly spaced root system; and ii) the same root pattern persisting long enough to allow band formation. Neither condition is likely in most soils. Root distributions do not show a regular structure that mirrors the observed patterns (SI Appendix, Fig. S9). Even if such regular structure existed, roots are highly dynamic (63) so as to allow plants to rapidly adjust root structure to shifting soil conditions and to compete for limited resources (64). Furthermore, while our study site is dominated by the same pine species, iron band patterns are very patchy across the landscape, indicating that drivers other than plants are important. Nevertheless, root structure commonly creates irregular redoximorphic features. For instance, wetland plants transport O₂ to their roots (65, 66), forming orange iron plaque on the root surface ("mottles") (4, 5, 67) (Fig. 1F), while the rhizosphere of upland plants can turn soil gray (3) (Fig. 1G). Formation of such redoximorphic features templating root structure is rapid (3, 67), consistent with our model results indicating that the root template mechanism forms patterning in a much shorter period than do other mechanisms (Fig. 2).

Rocks can exhibit rhythmic precipitate bands, i.e., Liesegang bands (or rings) (68). They result from a dissolved reactant diffusing from one end of a system into a reservoir of another dissolved reactant, with the precipitate bands progressively forming in the wake of a propagating reaction front (14). While looking like Liesegang bands, soil iron bands are unlikely formed by this mechanism. Wetland soils may contain a reservoir of dissolved Fe(II) (69).

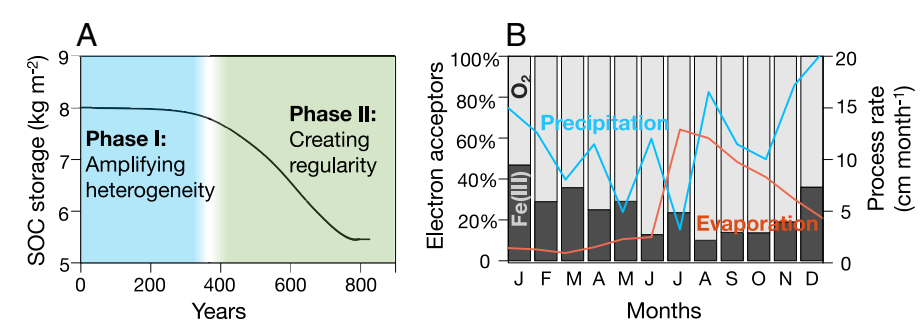


Fig. 6. (A) Model predicted a reduction of ~30% in the soil organic carbon (SOC) storage capacity in the pattern formation zone (between 1.0 and 1.8 m of soil depths) over the 900-y pattern forming period. (B) Model-simulated percent of SOC oxidized by O2 vs. by Fe(III) by month in a representative wet year at the Calhoun Experimental Forest (South Carolina). Monthly rainfall and evaporation rate (cm per month) are aggregated from the daily rate monitored at the study site between July 1, 2018, and June 30, 2019.

When O₂ diffuses from the air-soil interface into saturated soils, Fe(III) bands might form. However, in addition to O₂ diffusing from the upper boundary, hydrophyte roots transport O2 to roots and part of O₂ diffuses from the rhizosphere to soils throughout the system. These processes likely interrupt the band-forming reaction front. For upland soils, concentration of dissolved Fe(II) is typically low (58) and the highly dynamic redox cycling can frequently interrupt the propagation of the precipitation front.

Why Regular Iron Bands Might Be Rare? While iron redoximorphic features are common in soils, regular iron banding is rare. This likely has to do with the intricate coordination of climatic, soil, and ecological conditions required for regular pattern formation. Upland soils are often well aerated. Even in subtropical forests such as our study site, the marked seasonality of rainfall and temperature restricts anoxic conditions to relatively brief periods in winter/spring of wet years, when evapotranspiration is low and organic acid production is high from the previously years leaffall (58, 70) (SI Appendix, Fig. S6). In addition, soil moisture is sensitive to local factors, e.g., topography (51); hence, regular patterns can be patchy across a landscape. For example, no iron banding appears in a soil pit just 400 m from our site (Fig. 1). While anoxic conditions are more common in wetter regions, prolonged anoxic periods might accelerate Fe leaching, especially in soils with rich organic acids (71), limiting pattern formation. Moreover, while redox fluctuations can increase Fe(III) crystallinity, as is the case at our study site evidenced by field measurements (4, 39) and experiments (38), redox fluctuations can also decrease Fe(III) crystallinity under conditions favoring the formation of short-range-ordered Fe(III) oxides (24, 27, 52, 72), for instance, high OM content, a low concentration of crystalline Fe minerals, and a fast oxidation rate (27, 52). Iron banding is likely therefore to be limited to areas where Fe(III) crystallinity and aggregation increases during redox fluctuations. This is more likely to occur in predominately oxic environments in regions of the soil with low OM and a high abundance of crystalline Fe(III) phase (38).

Furthermore, the formation of rhythmic iron bands requires the vertical alignment of soil water, clay, Fe(III), and root profiles. At our site, iron bands start at 40 to 50 cm below the depth where clay and Fe(III) content begin to rapidly increase (Fig. 4). This is also the soil depth where anoxic conditions develop due to a perched water table in the winter months of wet years (SI Appendix, Fig. S6). Clay accumulations often occur between 0.3 and 3 m depths (73), a range determined by parent material, soil development, hydrologic regime, and land use (74-76). Similarly, Fe concentration depth profiles are sensitive to many factors, e.g., groundwater table, topography-driven surface flow (77). Importantly, iron band

formation requires organic reductants, i.e., root proliferation, at deep soil layers ($> \sim 1$ m) to overlap with the high-clay, high-Fe zone. At our site, fine roots of loblolly pine are present even at 4-m depth (74). At further deeper soil depths, low decomposable OM limits Fe(III) reduction. Overall, B horizons are the most likely zone for iron banding formation, and all reported iron bands occur in B horizons (4–6) (*SI Appendix*, Table S1).

Role of Environmental Variability. Environmental variability is common to ecosystems worldwide; however, its role in spatial selforganization remains understudied. Environmental oscillations have been shown to be critical in pattern formation via the phase separation principle (78-80). This study exemplifies the significance of temporal variability in Turing morphogenesis. Redox fluctuations induce clay dispersion/coagulation and alter Fe(III) crystallinity (24, 25, 81, 82). The environmental regime further dictates temporal intermittency of different patternforming processes and their relative rates over a given period, thereby determining the likelihood of pattern formation. In our study, the expansion of roots (an activator) operates continuously, while Fe(III) reduction and the transport of Fe(II) (an inhibitor) occur only intermittently. Thus, the formation of iron bands requires that root expansion be at least three orders of magnitude slower than Fe(II) diffusion (Fig. 7). In a drier climate, an even smaller D_b is requisite. Root extension of *Pinus taeda* at our site is slow compared to that of many subtropical trees (83). We estimated its root diffusion coefficient to be $\sim 1.8 \times 10^{-11} \text{ m}^2 \text{ s}^{-1}$ using the method in ref. 42 with reported P. taeda root extension rates (84). This estimate is very close to our model calibrated value (SI Appendix, Table S3).

To conclude, this study illustrates the critical role played by environmental variability in forming soil iron redox bands. Environmental variability prevails in ecosystems worldwide, directly controlling the operation of a wide range of chemical and physical processes and the timing and rates of many biological processes (e.g., phenology, life cycle). Given the significant role of temporal dynamics in pattern formation, projected changes in climatic variability might substantially alter many self-organized systems and shape the ecological functioning associated with the striking spatial patterns they display.

Methods

Modeling Redox Reactions in Upland Soils. We constructed a reactive transport model coupling soil water dynamics and soil redox reactions to investigate the mechanism of redox pattern formation. The upper boundary is the soil-air interface. We set the lower boundary at the soil depth of 4 m because the regional groundwater table is >5 m and redox patterns occur at soil depth <2 m. Model

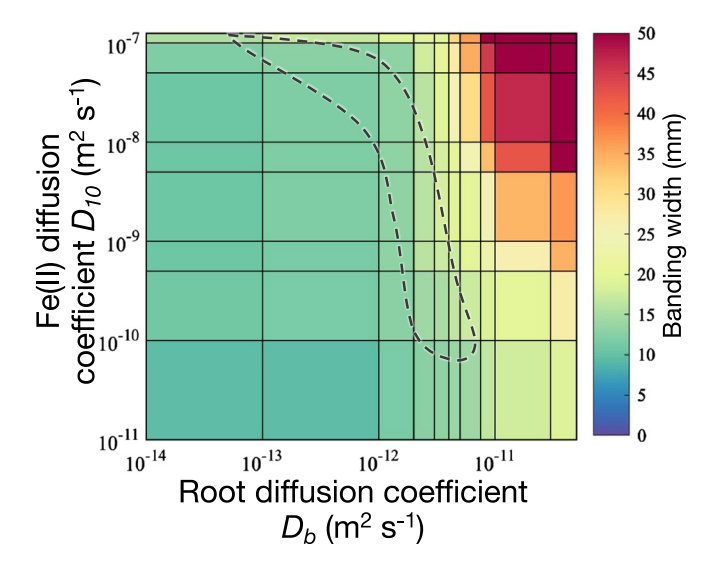


Fig. 7. Effect of diffusion coefficients of root biomass (D_b) and of Fe²⁺ (D_{10}) on the width of the regular iron bands in upland soils. The dash-line polygon delineates the area where bandwidth (average width of an orange band or a gray band, ~1.6 cm) is representative of that at our study site.

spatial resolution is 2 mm with a time step of 1 h, to capture the fine-scale spatial pattern and rapid chemical processes, respectively. The part of the model describing soil redox reactions includes six state variables, Fe(III), Fe(II), root biomass B, organic matter OM, clay, and oxygen, including dissolved oxygen O_{2l} and gaseous oxygen O_{2G} . Model parameters, their definitions, dimensions, and values are provided in SIAppendix, Table S3.

Rate of Fe(III) reduction is described in Results (Eq. **7**), and Fe(II) oxidation rate, $R_{\text{Fe(II)}}$ (mol m⁻³ d⁻¹) is as follows:

$$R_{Fe(II)} = k_{app} \left[Fe(II) \right] \frac{\left[O_{2L} \right]}{\left[O_{2L} \right] + H_{sO2}},$$
 [10]

where [Fe(II)] is the concentration of Fe(II) (mol m⁻³); k_{app} is the constant of Fe(II) oxidation rate (d⁻¹). Changes in Fe(II) is affected by chemical reactions, advection, and diffusion, as described in Eq. **6**. $D_{Fe(II)}$ is the diffusion coefficient (m² d⁻¹) of Fe(II) in soil pore water, which varies with soil water content, θ_L (85):

$$D_{Fe(l)} = D_{10} \frac{\theta_l^{7/3}}{\theta_s^2},$$
 [11]

where D_{10} is the molecular diffusivity of Fe(II) and θ_s is saturated soil water content. θ_s varies in space and time, with evolution of clay content, which is modeled in the Section "Soil Water Dynamics" below.

Change of root biomass density [B] (g m⁻³) (Eq. **3**) is affected by 1) root growth, G_B (Eq. **2**), 2) root respiration, R_B , 3) deposition of root residues, M_B , and 4) expansion to neighboring locations. Root respiration R_B (g m⁻³ d⁻¹) is assumed to be linear decay, affected by dissolved oxygen (86, 87):

$$R_B = k_r[B] \frac{[O_{2l}]}{[O_{2l}] + H_{BO2}},$$
 [12]

where k_r is respiration rate constant (d⁻¹). H_{BO2} is half-saturation constant to regulate the effect of O_{2L} on respiration (mol m⁻³). Deposition of root residues, M_B (g m⁻³ d⁻¹), is assumed to be a second-order function of biomass (88):

$$M_B = \frac{k_d [B]^2}{K_B},$$
 [13]

where k_d is root deposition constant (d⁻¹) and K_B (g m⁻³) is the carrying capacity of root biomass density, which decreases exponentially with soil depth (*SIAppendix*, Fig. S9). Notice that root biomass, B, is a lumped variable including roots, mycorrhizal fungal symbionts, and microbes, all contributing to the SOM pool (89).

We assume that deposition of ${\it B}$ is the primary source of SOM. The change of SOM is described as:

$$\frac{d[OM]}{dt} = \frac{M_B}{M_{om}} - R_{OMO} - \frac{1}{4} R_{Fe(III)},$$
 [14]

where M_{om} is molar mass of SOM, assuming 30 g mol⁻¹ for the generic formula of CH₂O. Rate of Fe(III) reduction, $R_{Fe(III)}$, is described by Eq. **7**. Rate of SOM oxidation by O₂, R_{OMO} (mol m⁻³ d⁻¹), is described as follows:

$$R_{OMO} = k_1 [OM] \frac{[O_{2l}]}{[O_{2l}] + H_{SO2}},$$
 [15]

Soil O_2 includes O_2 in dissolved form (O_{2L}) (mol O_2 per m³ soil water) and in gaseous form (O_{2G}) (mol O_2 per m³ soil void space). Soil O_2 is affected by O_2 diffusion in gas form and in dissolved form, advection of dissolved O_2 , root respiration, and oxidation of SOM and Fe(II):

$$\frac{\partial \left(\theta_{L}[O_{2L}] + \theta_{G}[O_{2G}]\right)}{\partial t} \\
= \theta_{L} \frac{\partial}{\partial z} \left(D_{1L} \frac{\partial [O_{2L}]}{\partial z}\right) + \theta_{G} \frac{\partial}{\partial z} \left(D_{1G} \frac{\partial [O_{2G}]}{\partial z}\right) \\
- \theta_{L} \frac{\partial}{\partial z} q_{L}[O_{2L}] - \frac{R_{B}}{M_{om}} - R_{OMO} - \frac{1}{4} R_{Fe (II)},$$
[16]

$$D_{1L} = D_{1L0} \frac{{\theta_L}^{7/3}}{{\theta_s}^2},$$
 [17]

where D_{1L} and D_{1G} are diffusion coefficients (m² s⁻¹) of O_{2L} and O_{2G} . D_{1L} varies with soil water content (Eq. **17**). θ_G represents soil gas content (m³ m⁻³). θ_G changes in space and time and is modeled in the Section "Soil Water Dynamics" below. D_{1L0} is the molecular diffusivity of O_{2L} . At 25 °C [O_{2L}] = 0.0318 [O_{2G}], according to Henry's law.

Initial Conditions, Boundary Conditions, and Numerical Solutions. It is not feasible to obtain the true initial condition of system. We assume that nearby sites in the same study area without redox patterns provide a good proxy for the initial condition. We use empirical measurements from these sites to initialize the model. Initial conditions for SOM are described by an exponential decay function of soil depth parameterized by field observations (*SI Appendix*, Figs. S9 and S10):

$$[SOM](z)_{init} = 775e^{-0.849z} (1 + r\beta),$$
 [18]

where r is a random number between -0.5 and 0.5 to include stochasticity in the initial SOM and β controls the magnitude of stochasticity. We assume that SOM consists of 5% living (B) and 95% non-living parts (OM). Initial Fe(II) was set to be zero everywhere in the model domain. Initial O_{2L} is 0.273 mol m⁻³ everywhere, in equilibrium with the atmospheric O_2 . The initial Fe(III) and clay contents follow an empirical hump-shaped function with the peak at depth \sim 1.2 m, informed by field measurements (SIAppendix, Fig. S10). Fe(III) is \sim 45 mol m⁻³ in shallow soil layers (<0.4 m), and between 438 and 500 mol m⁻³ at the depth between 0.6 and 1.5 m. Between 0.4 and 0.6 m and below 1.5 m soil depth, Fe(III) is at the intermediate level (SIAppendix, Fig. S10). In natural environments, the structure, solubility, and reactivity of Fe(III) minerals vary greatly (38, 90), and the same is true for OM (91). For our purpose, we modeled Fe reactions without considering diverse forms of Fe(III) and OM. As such, in the model, Fe(III) and OM are allowed to be depleted in chemical reactions.

For the soil–air interface upper boundary, we set a constant 0.273 mol m $^{-3}$ for O_{2l} , and a constant 0 for Fe(II), by assuming that Fe(II) is instantaneously oxidized by atmospheric O_2 . Based on empirical measurements, a constant 1,162 g m $^{-3}$ root biomass density (B) was used for the upper boundary (4) and a constant zero was used for the lower boundary (SI Appendix, Fig. S9). For Fe(II) and O_{2l} , we used a constant zero flux as the lower boundary. The model is solved by the implicit finite difference method. An iterative method is used to address nonlinear dynamics (48).

Soil Water Dynamics. We modeled soil water flux (q_l) and water content (θ_l) dynamics by numerically solving the unsaturated flow equation—the mixed form Richards equation:

$$\frac{\partial \theta_l}{\partial t} = \frac{\partial}{\partial z} \left[K(h) \left(\frac{\partial h}{\partial z} + 1 \right) \right],$$
 [19]

where h is pressure head (m) and K is hydraulic conductivity (m s⁻¹). K is estimated following (92):

$$K(h) = K_s Se(h)^l \left[1 - \left(1 - Se(h)^{\frac{1}{m}} \right)^m \right]^2,$$
 [20]

$$Se(h) = (1 + |\alpha h|^n)^{-m},$$
 [21]

where K_s is saturated hydraulic conductivity (m s⁻¹), l is a pore connectivity parameter (93), α , m, and n are semi-empirical fitting parameters of soil water retention curve (m = 1–1/n). K_s , α , and n are sensitive to soil texture, and soil texture, specifically clay content, evolves via clay dispersion/coagulation during iron redox oscillations. We allow K_s , α , and n to be a function of the evolving clay content (SIAppendix, Text S1). As such, our model captures the evolution of soil texture, which then affects soil water flux and content.

The Richards equation was solved using a mass-conservative finite difference method (94, 95). Due to the nonlinear nature of this equation, we employed Picard iteration and dynamic time step to ensure convergence of the solution at every time step. We applied daily rainfall and evapotranspiration observed between July 1, 2018, and July 1, 2019, at our study site as the climatic forcing (Fig. 6B). The year 2018-2019 was chosen because anoxic conditions occurred only in this year based on continuous field monitoring of soil water content and $\rm O_2$ between 2016 and 2020 (SI Appendix, Fig. S6). This year's rainfall and evapotranspiration rates were repeated yearly in our simulations. A flux equal to the observed evapotranspiration minus rainfall depth is imposed as the dynamic upper boundary. When the calculated head (h) at the soil-air interface is > 0, the model assumes the existence of surface runoff during heavy rainfall periods, in which case, the upper boundary switches to a constant head of 0. We used free drainage (i.e., $\partial h/\partial z = 0$) for the lower boundary condition and h = -1 m as the initial condition.

Solution of this model describes dynamic pressure head h of each computational grid. We used Eqs. **21** and **22** to solve dynamic Se and θ_L , respectively. Darcy's law was used to estimate spatially and temporally varying q_L :

$$\theta_L = \theta_r + (\theta_s - \theta_r) Se,$$
 [22]

$$q_L = -K \left(\frac{\partial h}{\partial z} + 1 \right),$$
 [23]

where θ_r is residual water content. θ_r and θ_s vary with soil texture—in our study, evolving clay content (*SI Appendix*, *Text* S1).

Numerical Experiments. To distinguish among alternative hypotheses of pattern formation, we tested five model variants (Fig. 2). 1) To test the mechanism of coupled amplifying SDFs and threshold-dependent SDFs, we ran the full model

- L. E. Moody, R. C. Graham, Geomorphic and pedogenic evolution in coastal sediments, central California. Geoderma 67, 181–201 (1995).
- S. K. Gangopadhyay, T. Bhattacharyya, D. Sarkar, Hydromorphic soils of Tripura: Their pedogenesis and characteristics. Curr. Sci. 108, 984–993 (2015).
- M. J. Vepraskas, "Morphological features of seasonally reduced soils" in Wetland Soils: Genesis, Hydrology, Landscapes, and Classification, J. L. Richardson, M. J. Vepraskas, Eds. (Lewis Publisher, Boca Raton, FL, 2000), pp. 163–182.
- R. L. Fimmen et al., Fe-C redox cycling: A hypothetical Rhizogenic that drives crustal mechanism biogeochemical in upland soils eathering. Biogeochemistry 87, 127–141 (2008).
- M. Schulz et al., Structured heterogeneity in a marine terrace chronosequence: Upland mottling. Vadose Zo. J. 15, 1–14 (2016).
- R. MacEwan, P. Dahlhaus, J. Fawcett, H. Lin, Hydropedology, Geomorphology, and Groundwater Processes in Land Degradation: Case Studies in South West Victoria, Australia (Academic Press, San Diego, 2012), pp. 449–481.
- D. Richter, N. Oh, R. Fimmen, J. Jackson, "The Rhizosphere and soil formation" in The Rhizoshpere an Ecological Perspective, Z. G. Cardon, J. L. Whitbeck, Eds. (Elsevier, MA., 2007), pp. 179–200.
- M. Rietkerk, S. C. Dekker, P. C. de Ruiter, J. van de Koppel, Self-organized patchiness and catastrophic shifts in ecosystems. *Science* 305, 1926-1929 (2004).

described above. 2) To test whether the amplifying SDFs alone can generate iron banding, we turned off processes describing threshold-dependent root responses to Fe(III), by removing $f_{Fe(III)}$ in Eq. 2. 3) To test whether the threshold-dependent SDFs alone can produce iron banding, we turned off the amplifying SDFs by removing Se in Eq. 7; 4) To test the mechanism of monotonic SDFs based on root responses to soil moisture, we turned off both the amplifying SDFs and threshold-dependent SDFs, by removing Se in Eq. 7 and replacing $f_{Fe(III)}$ in Eq. 2 with Se². Lastly, 5) to test the hypothesis that the iron banding is caused by a preexisting root structure, we prescribed regularly distributed root biomass and SOM as model initial conditions (SI Appendix, Fig. S7). The carrying capacity K_B is set to the initial distribution of SOM, to allow the root biomass to maintain the same regular distribution over time. All SDFs were turned off in the model, and the root diffusion term was removed from the biomass equation ($D_b = 0$ in Eq. 3). For each mechanism, we determined the pattern formation time. Pattern formation time is defined as the time it takes to form relatively stable patterns with Fe(III) content in the gray bands reaching the observed value in gray bands at our study site (138 mol m⁻³; SI Appendix, Table S2). Simulated patterns, including vertical distributions of Fe(III), B, OM, and clay content, are compared with the patterns observed in the field to determine the most plausible mechanism. Lastly, to test the effect of climatic and soil conditions on the emergence of regular iron bands, we manipulated annual rainfall regime and soil clay content in the model (SI Appendix, Text S2).

Estimating the Effect of Regular Iron Band Formation on Soil Carbon Storage. We first digitized photos of iron band patterns at our site (Fig. 1D) to quantify the width of gray and of orange bands. Then, we calculated the total carbon storage in the pattern formation zone (between 1.0 m and 1.8 m) by multiplying the width by the measured band-specific SOC content. This calculated carbon storage was compared with the carbon storage in the same zone from a nearby site without iron banding. This allows us to infer the percent reduction in carbon storage attributable to pattern formation. Furthermore, with the model, we compared the difference of total carbon in the initial condition and in the steady state to calculate the percent change in carbon storage by pattern formation. Since we used the SOC measured at the site without banding as the model initial condition, we expect that the percent change of carbon storage between the initial condition and the steady state to be statistically similar to the percent change between the sites with and without banding.

Data, Materials, and Software Availability. There are no data underlying this work.

ACKNOWLEDGMENTS. We thank Stuart G. Fisher for discussions that significantly improved this paper. This research was supported by NSF grant DEB #2320296 awarded to X.D., grant DEB #2241389 awarded to A.T., and grant EAR-1331846 awarded to D.D.R. We thank the Sumter National Forest of the United States Forest Service for decades of collaboration.

Author affiliations: ^aDepartment of Environmental Science and Policy, University of California, Davis, CA 95616; ^bEarth and Climate Sciences Division, Nicholas School of the Environment, Duke University, Durham, NC 27708; and ^cDepartment of Crop and Soil Sciences, University of Georgia, Athens, GA 30602

- M. Rietkerk et al., Evasion of tipping in complex systems through spatial pattern formation. Science 374, eabj0359 (2021).
- Q.-X. Liu et al., Phase separation explains a new class of self-organized spatial patterns in ecological systems. Proc. Natl. Acad. Sci. U.S.A. 110, 11905–11910 (2013).
- C. E. Tarnita et al., A theoretical foundation for multi-scale regular vegetation patterns. Nature 541, 398-401 (2017).
- M. Rietkerk, J. van de Koppel, Regular pattern formation in real ecosystems. Trends Ecol. Evol. 23, 169–175 (2008).
- C. A. Klausmeier, Regular and irregular patterns in semiarid vegetation. Science 284, 1826–1828 (1999).
- I. L'Heureux, Self-organized rhythmic patterns in geochemical systems. Philos. Trans. R. Soc. A Math. Phys. Eng. Sci. 371, 20120356 (2013).
- R. Sultan, P. Ortoleva, F. DePasquale, P. Tartaglia, Bifurcation of the Ostwald-Liesegang supersaturation-nucleation-depletion cycle. *Earth-Sci. Rev.* 29, 163–173 (1990).
- A. M. Turing, The chemical basis of morphogenesis. Philos. Trans. R. Soc. Lond. B. Biol. Sci. 237, 37–72 (1952).
- R. C. van de Vijsel et al., Estuarine biofilm patterns: Modern analogues for Precambrian selforganisation. Earth Surf. Process. Landforms 45, 1141–1154 (2020).

- 18. J. van de Koppel et al., Experimental evidence for spatial self-organization and its emergent effects in mussel bed ecosystems. Science 322, 739-742 (2008).
- M. Rietkerk, S. C. Dekker, M. J. Wassen, A. W. M. Verkroost, M. F. P. Bierkens, A putative mechanism for bog patterning. Am. Nat. 163, 699-708 (2004).
- M. Rietkerk et al., Self organization of vegetation in arid ecosystems. Am. Nat. 160, 525-530
- 21. Q.-X. Liu, E. J. Weerman, P. M. J. Herman, H. Olff, J. van de Koppel, Alternative mechanisms alter the emergent properties of self-organization in mussel beds. Proc. R. Soc. B Biol. Sci. 279, 2744-2753 (2012).
- L. Cheng et al., Atmospheric CO2 enrichment facilitates cation release from soil. Ecol. Lett. 13, 22. 284-291 (2010).
- C. S. O'Connell, L. Ruan, W. L. Silver, Drought drives rapid shifts in tropical rainforest soil 23 biogeochemistry and greenhouse gas emissions. Nat. Commun. 9, 1348 (2018).
- 24 A. Thompson, O. A. Chadwick, D. G. Rancourt, J. Chorover, Iron-oxide crystallinity increases during soil redox oscillations. Geochim. Cosmochim. Acta 70, 1710-1727 (2006).
- A. Thompson, O. A. Chadwick, S. Boman, J. Chorover, Colloid mobilization during soil iron redox oscillations. Environ. Sci. Technol. 40, 5743-5749 (2006).
- R. Kretzschmar, H. Holthoff, H. Sticher, Influence of pH and humic acid on coagulation kinetics of kaolinite: A dynamic light scattering study. J. Colloid Interface Sci. 202, 95-103 (1998).
- P. Winkler et al., Contrasting evolution of iron phase composition in soils exposed to redox fluctuations. Geochim. Cosmochim. Acta 235, 89-102 (2018).
- C. I. Steefel, A. C. Lasaga, A coupled model for transport of multiple chemical species and kinetic precipitation/dissolution reactions with application to reactive flow in single phase hydrothermal systems. Am. J. Sci. **294**, 529–592 (1994).
- K. Maher, C. I. Steefel, A. F. White, D. A. Stonestrom, The role of reaction affinity and secondary minerals in regulating chemical weathering rates at the Santa Cruz Soil Chronosequence, California. Geochim. Cosmochim. Acta 73, 2804-2831 (2009).
- $K.\ Maher, C.\ I.\ Steefel,\ D.\ J.\ De Paolo,\ B.\ E.\ Viani,\ The\ mineral\ dissolution\ rate\ conundrum:\ Insights$ from reactive transport modeling of U isotopes and pore fluid chemistry in marine sediments. Geochim. Cosmochim. Acta 70, 337-363 (2006).
- H. Eswaran, F. De Coninck, T. Varghese, Role of plinthite and related forms in soil degradation. Adv. Soil Sci. **11**, 109-127 (1990).
- L. Zhao et al., Formation of plinthite mediated by redox fluctuations and chemical weathering intensity in a Quaternary red soil, southern China. Geoderma 386, 114924 (2021).
- M. Aide, Z. Pavich, M. E. Lilly, R. Thornton, W. Kingery, Plinthite formation in the coastal plain region of Mississippi. Soil Sci. 169, 613-623 (2004).
- R. E. Haling et al., Root hairs improve root penetration, root-soil contact, and phosphorus acquisition
- in soils of different strength. J. Exp. Bot. 64, 3711-3721 (2013). E. Oleghe, M. Naveed, E. M. Baggs, P. D. Hallett, Plant exudates improve the mechanical conditions
- for root penetration through compacted soils. *Plant Soil* **421**, 19–30 (2017).

 C. W. Childs, R. W. P. Palmer, C. W. Ross, Thick iron oxide pans in soils of Taranaki, Zew Zealand. 36.
- Aust. J. Soil Res. 28, 245-257 (1990). J. E. Cairns, A. Audebert, J. Townend, A. H. Price, C. E. Mullins, Effect of soil mechanical impedance
- on root growth of two rice varieties under field drought stress. Plant Soil 267, 309-318 (2004). C. Chen, A. Thompson, The influence of native soil organic matter and minerals on ferrous iron
- oxidation. Geochim. Cosmochim. Acta 292, 254-270 (2021). C. Chen, D. Barcellos, D. D. Richter, P. A. Schroeder, A. Thompson, Redoximorphic Bt horizons of the Calhoun CZO soils exhibit depth-dependent iron-oxide crystallinity. J. Soils Sediments 19, 785-797
- H. Lu, W. Yuan, X. Chen, A processes-based dynamic root growth model integrated into the
- ecosystem model. J. Adv. Model. Earth Syst. 11, 4614-4628 (2019).
- A. G. Bengough, B. M. McKenzie, P. D. Hallett, T. A. Valentine, Root elongation, water stress, and mechanical impedance: A review of limiting stresses and beneficial root tip traits. J. Exp. Bot. 62, 59-68 (2011).
- M. L. Cain, Models of clonal growth in Solidago altissima. J. Ecol. 78, 27-46 (1990)
- M. Rietkerk et al., Self-organization of vegetation in arid ecosystems. Am. Nat. 160, 524-530 (2002).
 - L. Stolze et al., Aerobic respiration controls on shale weathering. Geochim. Cosmochim. Acta 340, 172-188 (2023).
- E. E. Roden, R. G. Wetzel, Kinetics of microbial Fe (III) oxide reduction in freshwater wetland sediments. Limnol. Oceanogr. 47, 198-211 (2002).
- B. Ginn, C. Meile, J. Wilmoth, Y. Tang, A. Thompson, Rapid iron reduction rates are stimulated by highamplitude redox fluctuations in a tropical forest soil. Environ. Sci. Technol. 51, 3250-3259 (2017).
- S. J. Hall, W. H. McDowell, W. L. Silver, When wet gets wetter: Decoupling of moisture, redox biogeochemistry, and greenhouse gas fluxes in a humid tropical forest soil. Ecosystems 16, 576-589 (2013).
- P. Van Cappellen, Y. Wang, Cycling of iron and manganese in surface sediments: A general theory for the coupled transport and reaction of carbon, oxygen, nitrogen, sulfur, iron, and manganese. Am. J. Sci. 296, 197-243 (1996).
- 49. C. Hodges, E. King, J. Pett-Ridge, A. Thompson, Potential for iron reduction increases with rainfall in montane basaltic soils of hawaii. Soil Sci. Soc. Am. J. 82, 176-185 (2018).
- K. A. Weber, L. A. Achenbach, J. D. Coates, Microorganisms pumping iron: Anaerobic microbial iron oxidation and reduction. Nat. Rev. Microbiol. 4, 752-764 (2006).
- $D.\ Barcellos,\ C.\ S.\ O'connell,\ W.\ Silver,\ C.\ Meile,\ A.\ Thompson,\ Hot\ spots\ and\ hot\ moments\ of\ soil$ moisture explain fluctuations in iron and carbon cycling in a humid tropical forest soil. Soil Syst. 2, 1-22 (2018)
- 52. A. Thompson, D. G. Rancourt, O. A. Chadwick, J. Chorover, Iron solid-phase differentiation along a redox gradient in basaltic soils. Geochim. Cosmochim. Acta 75, 119-133 (2011).
- S. Bonneville, P. Van Cappellen, T. Behrends, Microbial reduction of iron(III) oxyhydroxides: Effects of mineral solubility and availability. Chem. Geol. 212, 255-268 (2004).
- 54. J. Yan, V. Lazouskaya, Y. Jin, Soil colloid release affected by dissolved organic matter and redox conditions. Vadose Zo. J. 15, 1-10 (2016).

- 55. J. N. Ryan, P. M. Gschwend, Colloid mobilization in two Atlantic coastal plain aquifers: Field studies. Water Resour. Res. 26, 307-322 (1990).
- J. N. Ryan, P. M. Gschwend, Effect of solution chemistry on clay colloid release from an iron oxide-coated aquifer sand. Environ. Sci. Technol. 28, 1717-1726 (1994).
- J. Zhuang, Y. Jin, M. Flury, Comparison of hanford colloids and kaolinite transport in porous media. Vadose Zo. J. 3, 395-402 (2004).
- S. Calabrese, D. Barcellos, A. Thompson, A. Porporato, Theoretical constraints on Fe reduction rates in upland soils as a function of hydroclimatic conditions. J. Geophys. Res. Biogeosci. 125, e2020JG005894 (2020).
- M. A. Gil, Unity through nonlinearity: A unimodal coral-nutrient interaction. *Ecology* **94**, 1871–1877 (2013)
- J. S. Rosenfeld, Developing flow-ecology relationships: Implications of nonlinear biological responses for water management. *Freshw. Biol.* **62**, 1305–1324 (2017). 60.
- A. Pervez, P. P. Singh, H. Bozdoğan, Ecological perspective of the diversity of functional responses. Eur. J. Environ. Sci. 8, 97-101 (2018).
- $E.\,I.\,Vanguelova,\,S.\,\,Nortcliff,\,A.\,\,J.\,\,Moffat,\,F.\,\,Kennedy,\,Morphology,\,biomass\,and\,\,nutrient\,status\,\,of\,\,Morphology,\,biomass\,and\,\,nutrient\,\,status\,\,of\,\,Morphology,\,Morphology,\,Biomass\,\,Archivertical Science (Control of Control of Control$ fine roots of Scots pine (Pinus sylvestris) as influenced by seasonal fluctuations in soil moisture and soil solution chemistry. Plant Soil 270, 233-247 (2005).
- K. S. Pregitzer et al., Fine root architecture of nine North American trees. Ecol. Monogr. 72, 293-309
- C. J. Bilbrough, M. M. Caldwell, The effects of shading and N status on root proliferation in nutrient patches by the perennial grass Agropyron desertorum in the field. Oecologia 103, 10-16 (1995).
- J. Liu, X. Leng, M. Wang, Z. Zhu, Q. Dai, Iron plaque formation on roots of different rice cultivars and the relation with lead uptake. Ecotoxicol. Environ. Saf. 74, 1304-1309 (2011).
- T. Matsui, T. Tsuchiya, A method to estimate practical radial oxygen loss of wetland plant roots. Plant Soil **279**, 119-128 (2006).
- M. J. Vepraskas, J. L. Richardson, J. P. Tandarich, Dynamics of redoximorphic feature formation under controlled ponding in a created riverine wetland. *Wetlands* **26**, 486–496 (2006).
- R. Liesegang, Chemische fernwirkung. Photogr. Arch. 801, 331-336 (1896).
- K. L. Sahrawat, Iron toxicity in wetland rice and the role of other nutrients. J. Plant Nutr. 27, 1471-1504 (2004)
- C. Hodges, J. Mallard, D. Markewitz, D. Barcellos, A. Thompson, Seasonal and spatial variation in the potential for iron reduction in soils of the Southeastern Piedmont of the US. Catena 180, 32-40 (2019).
- C. Colombo, G. Palumbo, J. Z. He, R. Pinton, S. Cesco, Review on iron availability in soil: Interaction of Fe minerals, plants, and microbes. J. Soils Sediments 14, 538-548 (2014).
- A. J. Coby, F. Picardal, E. Shelobolina, H. Xu, E. E. Roden, Repeated anaerobic microbial redox cycling of iron. Appl. Environ. Microbiol. 77, 6036-6042 (2011).
- H. O. Buckman, N. C. Brady, The nature and properties of soils. Soil Sci. 90, 212 (1960).
- D. D. Richter, D. Markewitz, How deep is soil? Bioscience 45, 600-609 (1995).
- S. Calabrese, D. D. Richter, A. Porporato, The formation of clay-enriched horizons by lessivage. Geophys. Res. Lett. 45, 7588-7595 (2018).
- R. C. Ryland, A. Thompson, L. A. Sutter, D. Markewitz, Mapping depth to the argillic horizon on historically farmed soil currently under forests. Geoderma 369, 114291 (2020).
- Z. Fekiacova, S. Pichat, S. Cornu, J. Balesdent, Inferences from the vertical distribution of Fe isotopic compositions on pedogenetic processes in soils. Geoderma 209-210, 110-118 (2013).
- 78. M. A. Kessler, B. T. Werner, Self-organization of sorted patterned ground. Science 299, 380-383 (2003).
- M. A. Kessler, A. B. Murray, B. T. Werner, B. Hallet, A model for sorted circles as self-organized patterns. J. Geophys. Res. Solid Earth 106, 13287-13306 (2001).
- A. Li et al., Ice needles weave patterns of stones in freezing landscapes. Proc. Natl. Acad. Sci. U.S.A. 118, e2110670118 (2021).
- V. Vogelsang, K. Kaiser, F. E. Wagner, R. Jahn, S. Fiedler, Transformation of clay-sized minerals in soils exposed to prolonged regular alternation of redox conditions. Geoderma 278, 40-48 (2016).
- 82. M. Z. Afsar, J. Yan, B. Vasilas, Y. Jin, Redox oscillations destabilize and mobilize colloidal soil organic carbon. Sci. Total Environ. 864, 161153 (2023).
- O. J. Valverde-Barrantes, J. W. Raich, A. E. Russell, Fine-root mass, growth and nitrogen content for six tropical tree species. Plant Soil 290, 357-370 (2007).
- J. S. King et al., Below-ground carbon input to soil is controlled by nutrient availability and fine root dynamics in loblolly pine. New Phytol. **154**, 389–398 (2002).
- R. J. Millington, J. P. Quirk, Permeability of porous solids. Trans. Faraday Soc. 57, 1200–1207 (1961).
- A. Porporato, P. D'Odorico, F. Laio, I. Rodriguez-Iturbe, Hydrologic controls on soil carbon and nitrogen cycles. I. Modeling scheme. Adv. Water Resour. 26, 45-58 (2003).
- S. Manzoni, A. Porporato, A theoretical analysis of nonlinearities and feedbacks in soil carbon and nitrogen cycles. Soil Biol. Biochem. 39, 1542-1556 (2007).
- N. F. Pelak, A. J. Parolari, A. Porporato, Bistable plant-soil dynamics and biogenic controls on the soil production function. Earth Surf. Process. Landforms 41, 1011-1017 (2016).
- D. L. Godbold et al., Mycorrhizal hyphal turnover as a dominant process for carbon input into soil organic matter. Plant Soil 281, 15-24 (2006).
- R. M. Cornell, U. Schwertmann, The Iron Oxides: Structure, Properties, Reactions, Occurrences, and Uses (Wiley-vch, Weinheim, 2003).
- J. Chen, B. Gu, R. A. Royer, W. D. Burgos, The roles of natural organic matter in chemical and microbial reduction of ferric iron. Sci. Total Environ. 307, 167-178 (2003).
- M. T. van Genuchten, A closed-form equation for predicting the hydraulic conductivity of unsaturated soils. Soil Sci. Soc. Am. J. 44, 892 (1980).
- Y. Mualem, A new model for predicting the hydraulic conductivity of unsaturated porous media. Water Resour. Res. 12, 513-522 (1976).
- M. A. Celia, E. T. Bouloutas, R. L. Zarba, A general mass-conservative numerical solution for the unsaturated flow equation. Water Resour. Res. 26, 1483-1496 (1990).
- J. Simunek, M. T. Van Genuchten, M. Sejna, The HYDRUS-1D software package for simulating the one-dimensional movement of water, heat, and multiple solutes in variably-saturated media. Univ. California-Riverside Res. Rep. 3, 1-240 (2005).